The Journal of Chemical Physics | ARTICLE | scitation.org/journal/jcp

Effect of spin–orbit coupling on strong field ionization simulated with time-dependent configuration interaction

Cite as: J. Chem. Phys. 153, 244109 (2020); doi: 10.1063/5.0034807
Submitted: 22 October 2020 • Accepted: 4 December 2020 •
Published Online: 23 December 2020

Mi Kyung Lee, Paul Hoerner, Wen Li, and H. Bernhard Schlegel[a)]

AFFILIATIONS

Department of Chemistry, Wayne State University, Detroit, Michigan 48202, USA

[a)]Author to whom correspondence should be addressed: hbs@chem.wayne.edu

ABSTRACT

Time-dependent configuration interaction with a complex absorbing potential has been used to simulate strong field ionization by intense laser fields. Because spin–orbit coupling changes the energies of the ground and excited states, it can affect the strong field ionization rate for molecules containing heavy atoms. Configuration interaction with single excitations (CIS) has been employed for strong field ionization of closed shell systems. Single and double excitation configuration interaction with ionization (CISD-IP) has been used to treat ionization of degenerate states of cations on an equal footing. The CISD-IP wavefunction consists of ionizing single (one hole) and double (two hole/one particle) excitations from the neutral atom. Spin–orbit coupling has been implemented using an effective one electron spin–orbit coupling operator. The effective nuclear charge in the spin–orbit coupling operator has been optimized for Ar^+, Kr^+, Xe^+, HX^+ (X = Cl, Br, and I). Spin–orbit effects on angular dependence of the strong field ionization have been studied for HX and HX^+. The effects of spin–orbit coupling are largest for ionization from the π orbitals of HX^+. In a static field, oscillations are seen between the $^2\Pi_{3/2}$ and $^2\Pi_{1/2}$ states of HX^+. For ionization of HX^+ by a two cycle circularly polarized pulse, a single peak is seen when the maximum in the carrier envelope is perpendicular to the molecular axis and two peaks are seen when it is parallel to the axis. This is the result of the greater ionization rate for the π orbitals than for the σ orbitals.

I. INTRODUCTION

Strong field dynamics plays a central role in attosecond spectroscopy, which aims to study real-time electronic dynamics.[1] For molecules containing heavier atoms, relativistic effects can lead to important effects. For example, the dynamics of coherent superpositions of spin–orbit states in krypton and deuterium bromide have been observed experimentally.[2,3] The intense fields used in strong field studies can distort the electron density in a manner that cannot be treated by perturbation theory. Consequently, strong field electron dynamics must be simulated by quantum mechanical propagation of the electrons in the presence of the intense laser field. Theoretical methods for treating strong field electron dynamics have been reviewed recently.[1,4–7] While one and two electron systems can be treated accurately, systems with many electrons are still challenging to model. Some of the methods that have been used to simulate many electron systems include the strong field approximation (SFA), the single active electron (SAE) approximation, and time-dependent electronic structure methods. Some examples of time-dependent electronic structure methods for simulations of strong field ionizations in molecules include the multi-configuration self-consistent field (MCSCF), configuration interaction, and coupled cluster methods[8–34] and real-time integration of density functional theory.[35–43] In previous studies, we have used time-dependent configuration interaction (TDCI) with a complex absorbing potential to study the angular dependence of strong field ionization of various molecular systems.[14,20,21,26–30,32–34]

For molecules containing heavier atoms, relativistic effects can alter the relative energies of ground and excited electronic states.[44,45] However, simulating ionization by propagating relativistic four-component or two-component wavefunctions can be costly for molecular systems. Spin–orbit coupling is one of the important contributions that can be taken into account by adding a term to the non-relativistic Schrödinger equation.[46] The spin–orbit coupling operator from the Breit–Pauli Hamiltonian consists of one and two electron terms. For heavy atoms, the one electron term dominates, and the expensive two electron terms can be approximated by using a one electron operator based on a mean field or effective nuclear charge approach.[47]

Except for the very heavy elements, spin–orbit contributions are small compared to other terms in the Schrödinger equation. The spin–orbit effects are most pronounced for coupling between degenerate or closely spaced states with different z-components of the spin and angular momentum. Consequently, state-averaged MCSCF and multi-reference configuration interaction (MRCI) calculations are often used to evaluate spin–orbit coupling.[48–55] Coupled cluster methods have been used to include dynamic electron correlation and obtain more accurate spin–orbit coupling constants.[56–69] However, the MCSCF, MRCI, and coupled cluster methods are difficult to extend to the large number of states typically needed for simulating strong field ionization. We have used configuration interaction with all single excitations (CIS) to generate the many thousands of states needed for simulating strong field ionization.[14,20,21,26–30,32–34] Spin–orbit matrix elements for CIS have been presented in a convenient form by Bellonzi and co-workers.[70] CIS with spin–orbit coupling based on a spin-restricted Hartree–Fock reference determinant is suitable for simulating ionization of closed shell systems. For corresponding calculations on open-shell systems such as radical cations, spin-unrestricted Hartree–Fock would be most convenient, but this can artificially break the degeneracy between states that interact by spin–orbit coupling. As an alternative to state-averaged MCSCF calculations, single and double excitation configuration interaction with ionization (CISD-IP) can be used to treat open shell systems with degenerate ground states. Golubeva and co-workers[71] have presented the matrix elements for CISD-IP in a readily programmable form. We have implemented this approach to model sequential double ionization of neon and acetylene.[34]

In the present paper, we combine spin–orbit coupling with CISD-IP to simulate strong field ionization of open-shell systems with degenerate ground states. We also implement CIS with spin–orbit coupling for strong field ionization of closed shell systems. In Sec. II, we present the matrix elements for spin–orbit coupling for CIS and CISD-IP in an easy to code form. In Sec. III, we study the effect of spin–orbit coupling on the ionization rates for hydrogen halide cations HCl^+, HBr^+, and HI^+.

II. METHODS

The electronic wavefunction is propagated with the time-dependent Schrödinger equation including the Breit–Pauli spin–orbit coupling operator, $\mathbf{V}^{SOC}$ (atomic units are used throughout this paper),

$$i\frac{\partial}{\partial t}\Psi_{el}(t) = [\hat{\mathbf{H}}_{el} + \hat{\mathbf{V}}^{SOC} - \hat{\mu}\cdot\vec{E}(t) - i\,\hat{\mathbf{V}}^{absorb}]\Psi_{el}(t), \quad (1)$$

where $\hat{H}_{el}$ is the field-free non-relativistic electronic Hamiltonian. The spin–orbit coupling term is approximated by an effective one electron spin–orbit coupling operator,[46]

$$\hat{\mathbf{V}}^{SOC} = -\frac{\alpha_0^2}{2}\sum_A \frac{Z_A^{eff}}{i}\frac{(\mathbf{r}-\mathbf{r}_A)\times\nabla}{|\mathbf{r}-\mathbf{r}_A|^3}. \quad (2)$$

Suitable values for Z^{eff} have been reported by Koseki, Gordon, and co-workers[48–51] and by Chiodo and Russo.[72] The interaction with the intense electric field is treated in the semiclassical dipole approximation, where $\widehat{\mu}$ is the dipole operator and $\vec{E}$ is the electric field. Ionization is modeled with a complex absorbing potential (CAP) $i\mathbf{V}^{absorb}$ as described in earlier papers.[14,20,21,26–30,32–34] The time-dependent wavefunction is expanded in terms of the ground and singly excited states of the field-free non-relativistic Hamiltonian.

For simulations involving closed shell systems with CIS and spin–orbit coupling, the wavefunction includes all singlet and triplet singly excited configurations (all $\alpha\to\alpha$, $\beta\to\beta$, $\alpha\to\beta$, $\beta\to\alpha$ excited determinants),

$$\begin{aligned}\Psi_{el}(t) &= \sum_{I=0} C_I(t)|\Psi_I\rangle \\ &= c_0\Psi_0 + \sum_{ia} c_i^a\Psi_i^a + \sum_{\bar{i}\bar{a}} c_{\bar{i}}^{\bar{a}}\Psi_{\bar{i}}^{\bar{a}} + \sum_{i\bar{a}} c_i^{\bar{a}}\Psi_i^{\bar{a}} + \sum_{\bar{i}a} c_{\bar{i}}^{a}\Psi_{\bar{i}}^{a},\end{aligned} \quad (3)$$

where i, j are occupied α molecular orbitals and a, b are unoccupied α molecular orbitals, while $\bar{i}, \bar{j}$ and $\bar{a}, \bar{b}$ are the corresponding β molecular orbitals. The matrix elements of the non-relativistic Hamiltonian for the singly excited configurations are

$$\begin{aligned}&\langle\Psi_0|\mathbf{H}_{el}|\Psi_0\rangle = E_{HF}, \quad \left\langle\Psi_0|\mathbf{H}_{el}|\Psi_i^a\right\rangle = 0, \\ &\left\langle\Psi_i^a|\mathbf{H}_{el}|\Psi_j^b\right\rangle = (E_{HF}+\varepsilon_a-\varepsilon_i)\delta_{ij}\delta_{ab} - \langle ja||ib\rangle\end{aligned} \quad (4)$$

for each of the spin cases in Eq. (3). The double bar integrals are

$$\langle rs||tu\rangle = \int dr_1 dr_2 \phi_r^*(r_1)\phi_s^*(r_2)\frac{1}{r_{12}}[\phi_t(r_1)\phi_u(r_2) - \phi_u(r_1)\phi_t(r_2)]. \quad (5)$$

The molecular orbital matrix elements of the effective one electron spin–orbit coupling operator are

$$\{V_{pq}^X, V_{pq}^Y, V_{pq}^Z\} = -\frac{\alpha_0^2}{2}\sum_A\frac{Z_A^{eff}}{i}\left\langle p\left|\frac{(\mathbf{r}-\mathbf{r}_A)\times\nabla}{|\mathbf{r}-\mathbf{r}_A|^3}\right|q\right\rangle, \quad (6)$$

where α_0 is the fine structure constant. The z-component of the one electron spin–orbit coupling matrix elements is non-zero for the $\alpha\alpha$ and $\beta\beta$ spin cases,

$$\begin{aligned}V_{pq}^Z &= -\frac{\alpha_0^2}{2}\sum_A\frac{Z_A^{eff}}{i}\left[\left\langle p\left|\frac{(x-x_A)}{|\mathbf{r}-\mathbf{r}_A|^3}\frac{\partial}{\partial y}\right|q\right\rangle - \left\langle p\left|\frac{(y-y_A)}{|\mathbf{r}-\mathbf{r}_A|^3}\frac{\partial}{\partial x}\right|q\right\rangle\right], \\ V_{\bar{p}\bar{q}}^Z &= \frac{\alpha_0^2}{2}\sum_A\frac{Z_A^{eff}}{i}\left[\left\langle \bar{p}\left|\frac{(x-x_A)}{|\mathbf{r}-\mathbf{r}_A|^3}\frac{\partial}{\partial y}\right|\bar{q}\right\rangle - \left\langle \bar{p}\left|\frac{(y-y_A)}{|\mathbf{r}-\mathbf{r}_A|^3}\frac{\partial}{\partial x}\right|\bar{q}\right\rangle\right].\end{aligned} \quad (7)$$

The x-component and y-component of the spin–orbit coupling operators can be combined to form raising and lowering operators; these matrix elements are non-zero for the $\alpha\beta$ and $\beta\alpha$ spin cases,

$$V_{p\bar{q}}^{X} = -\frac{\alpha_0^2}{2}\sum_A \frac{Z_A^{eff}}{i}\left[\left\langle p\left|\frac{(y-y_A)}{|\mathbf{r}-\mathbf{r}_A|^3}\frac{\partial}{\partial z}\right|\bar{q}\right\rangle - \left\langle p\left|\frac{(z-z_A)}{|\mathbf{r}-\mathbf{r}_A|^3}\frac{\partial}{\partial y}\right|\bar{q}\right\rangle\right],$$
$$V_{p\bar{q}}^{Y} = -\frac{\alpha_0^2}{2}\sum_A \frac{Z_A^{eff}}{i}\left[\left\langle p\left|\frac{(z-z_A)}{|\mathbf{r}-\mathbf{r}_A|^3}\frac{\partial}{\partial x}\right|\bar{q}\right\rangle - \left\langle p\left|\frac{(x-x_A)}{|\mathbf{r}-\mathbf{r}_A|^3}\frac{\partial}{\partial z}\right|\bar{q}\right\rangle\right], \tag{8}$$
$$V_{p\bar{q}}^{+} = V_{p\bar{q}}^{X} + \frac{1}{i}V_{p\bar{q}}^{Y}, \quad V_{\bar{p}q}^{-} = V_{\bar{p}q}^{X} - \frac{1}{i}V_{\bar{p}q}^{Y} = V_{q\bar{p}}^{+*}.$$

To simplify the notation, the matrix elements for the z-component of the one electron spin–orbit operator and for the raising/lowering operators can be assembled in a single matrix that covers all of the spin combinations for spin–orbit coupling,

$$\begin{aligned} V_{pq}^{SOC} &= V_{pq}^{Z} \text{ for } p \in \alpha, q \in \alpha \\ &= V_{\bar{p}\bar{q}}^{Z} \text{ for } p \in \beta, q \in \beta \\ &= V_{p\bar{q}}^{+} \text{ for } p \in \alpha, q \in \beta \\ &= V_{\bar{p}q}^{-} \text{ for } p \in \beta, q \in \alpha. \end{aligned} \tag{9}$$

The matrix elements for the effective one electron spin–orbit coupling operator for the singly excited configurations are

$$\langle\Psi_0|\mathbf{V}^{SOC}|\Psi_0\rangle = 0, \quad \langle\Psi_0|\mathbf{V}^{SOC}|\Psi_i^a\rangle = V_{ia}^{SOC},$$
$$\langle\Psi_i^a|\mathbf{V}^{SOC}|\Psi_j^b\rangle = V_{ab}^{SOC}\delta_{ij} - V_{ji}^{SOC}\delta_{ab} \tag{10}$$

for each of the spin cases in Eq. (3).

Open shell systems such as radical cations can be calculated with spin-unrestricted molecular orbitals. However, this does not treat the α and β orbitals equivalently. Alternatively, these systems can be calculated with the CISD-IP approach of Krylov and co-workers.[71] The time-dependent CISD-IP wavefunction is constructed using the molecular orbitals of the closed shell system and includes singly ionized configurations and singly excited, singly ionized configurations. As in the CIS case, the wavefunction for CISD-IP with spin–orbit coupling must include α → β and β → α excitations in addition to α → α and β → β excitations,

$$\Psi(t) = \sum_{I=0} C_I(t)|\Psi_I\rangle = \sum_x c_x\Psi_x + \sum_{\bar{x}} c_{\bar{x}}\Psi_{\bar{x}} + \sum_{iax} c_{ix}^a\Psi_{ix}^a + \sum_{ia\bar{x}} c_{i\bar{x}}^a\Psi_{i\bar{x}}^a$$
$$+ \sum_{\bar{i}\bar{a}x} c_{\bar{i}x}^{\bar{a}}\Psi_{\bar{i}x}^{\bar{a}} + \sum_{\bar{i}\bar{a}\bar{x}} c_{\bar{i}\bar{x}}^{\bar{a}}\Psi_{\bar{i}\bar{x}}^{\bar{a}} + \sum_{i\bar{a}x} c_{ix}^{\bar{a}}\Psi_{ix}^{\bar{a}} + \sum_{\bar{i}a\bar{x}} c_{\bar{i}\bar{x}}^{a}\Psi_{\bar{i}\bar{x}}^{a}, \tag{11}$$

where x, y are the ionized molecular orbitals ($i < x$ when i and x are of the same spin). The matrix elements of the non-relativistic Hamiltonian for the CISD-IP approach are

$$\langle\Psi_x|\mathbf{H}_{el}|\Psi_y\rangle = (E_{HF} - \varepsilon_x)\delta_{xy}, \quad \langle\Psi_x|\mathbf{H}_{el}|\Psi_{jy}^b\rangle = \langle jy||xb\rangle,$$
$$\langle\Psi_{ix}^a|\mathbf{H}_{el}|\Psi_{jy}^b\rangle = (E_{HF} + \varepsilon_a - \varepsilon_i - \varepsilon_x)\delta_{ij}\delta_{ab}\delta_{xy} + \langle yj||xi\rangle\delta_{ab}$$
$$- \langle ya||xb\rangle\delta_{ij} - \langle ja||ib\rangle\delta_{xy} + \langle ja||xb\rangle\delta_{iy} + \langle ya||ib\rangle\delta_{xj} \tag{12}$$

for each of the spin cases in Eq. (11). The corresponding matrix elements for the effective one electron spin–orbit operator are

$$\langle\Psi_x|\hat{\mathbf{V}}^{SOC}|\Psi_y\rangle = -V_{yx}^{SOC}, \quad \langle\Psi_x|\hat{\mathbf{V}}^{SOC}|\Psi_{jy}^b\rangle = V_{jb}^{SOC}\delta_{xy} - V_{yb}^{SOC}\delta_{xj},$$
$$\langle\Psi_{ix}^a|\hat{\mathbf{V}}^{SOC}|\Psi_{jy}^b\rangle = V_{ab}^{SOC}\delta_{ij}\delta_{xy} - V_{ji}^{SOC}\delta_{ab}\delta_{xy} - V_{yx}^{SOC}\delta_{ab}\delta_{ij}$$
$$+ V_{yi}^{SOC}\delta_{ab}\delta_{xj} + V_{jx}^{SOC}\delta_{ab}\delta_{iy} - V_{ab}^{SOC}\delta_{iy}\delta_{xj}. \tag{13}$$

As described in previous papers,[14,20,21,26–30,32–34] the absorbing potential for the molecule is constructed from spherical potentials centered on each atom and is equal to the minimum of the values of the atomic absorbing potentials. The spherical atomic absorbing potential begins at 3.5 times the van der Waals radius of each element (R_H = 9.544 bohrs, R_{Cl} = 13.052 bohrs, R_{Br} = 13.853 bohrs, R_I = 14.882 bohrs), rises quadratically to 5 hartree at approximately R + 14 bohrs, and turns over quadratically to 10 hartree at approximately R + 28 bohrs.

Simulations of strong field ionization were carried out with a seven cycle linearly polarized 800 nm (ω = 0.057 a.u.) pulse with a $\sin^2$ envelope,

$$\begin{aligned} &E(t) = E_{\max}\sin(\omega t/14)^2\cos(\omega t) && \text{for } 0 \le t \le 14\pi/\omega, \\ &E(t) = 0 && \text{for } t \ge 14\pi/\omega, \end{aligned} \tag{14}$$

and a two cycle circularly polarized 800 nm pulse in the xz plane with a $\sin^2$ envelope,

$$E_x(t) = E_{\max}\sin(\omega t/4)^2[-\cos(\omega t)\cos(\gamma) - \sin(\omega t)\sin(\gamma)],$$
$$Ez(t) = E_{\max}\sin(\omega t/4)^2[\cos(\omega t)\sin(\gamma) - \sin(\omega t)\cos(\gamma)] \tag{15}$$
$$\text{for } 0 \le t \le 4\pi/\omega, \quad E_z(t) = E_x(t) = 0 \text{ for } t \ge 4\pi/\omega.$$

Here, $E_{\max}$ is the maximum value for the electric field and γ determines the direction of the field at the maximum of the pulse. To obtain directional information for ionization, a static field was used instead of an oscillating field.[27,29,30,33] To avoid non-adiabatic excitations, the electric field is slowly ramped up to a constant value,

$$\begin{aligned} &E(t) = E_{\max}\left(1 - \left(1 - \tfrac{t}{t_{ramp}}\right)^4\right) && \text{for } 0 \le t \le t_{ramp}, \\ &E(t) = E_{\max} && \text{for } t \ge t_{ramp}, \end{aligned} \tag{16}$$

where t_{ramp} = 533 a.u. = 12.9 fs. The various pulse shapes are shown in Fig. 1.

The exponential of the Hamiltonian is used to propagate the time-dependent wavefunction. For a linearly polarized pulse, the Trotter factorization of the exponential is

$$\begin{aligned} \Psi(t+\Delta t) &= \exp(-i\hat{\mathbf{H}}\Delta t)\Psi(t), \\ \mathbf{C}(t+\Delta t) &= \exp(-i\mathbf{H}_{el}\Delta t/2)\exp(-\mathbf{V}^{absorb}\Delta t/2) \\ &\quad\times\mathbf{W}^T\exp(iE(t+\Delta t/2)\,\mathbf{d}\,\Delta t)\,\mathbf{W} \\ &\quad\times\exp(-\mathbf{V}^{absorb}\Delta t/2)\exp(-i\mathbf{H}_{el}\Delta t/2)\mathbf{C}(t), \end{aligned} \tag{17}$$

where $\mathbf{WDW}^T = \mathbf{d}$ are the eigenvalues and eigenvectors of the transition dipole matrix $\mathbf{D}$ in the field direction. The matrices $\exp(-i\mathbf{H}_{el}\Delta t/2)$, $\exp(-\mathbf{V}^{absorb}\Delta t/2)$, $\mathbf{W}$, and $\mathbf{d}$ need to be calculated only once at the beginning of the propagation because they are time independent. Likewise, the product $\mathbf{U} = \exp(-\mathbf{V}^{absorb}\Delta t/2)\,\mathbf{W}^T$ is formed once at the beginning of the propagation. The only time-dependent factor is $\exp(i\,E(t + \Delta t/2)\,\mathbf{d}\,\Delta t)$; this exponential can be calculated easily because $\mathbf{d}$ is a diagonal matrix. A propagation step

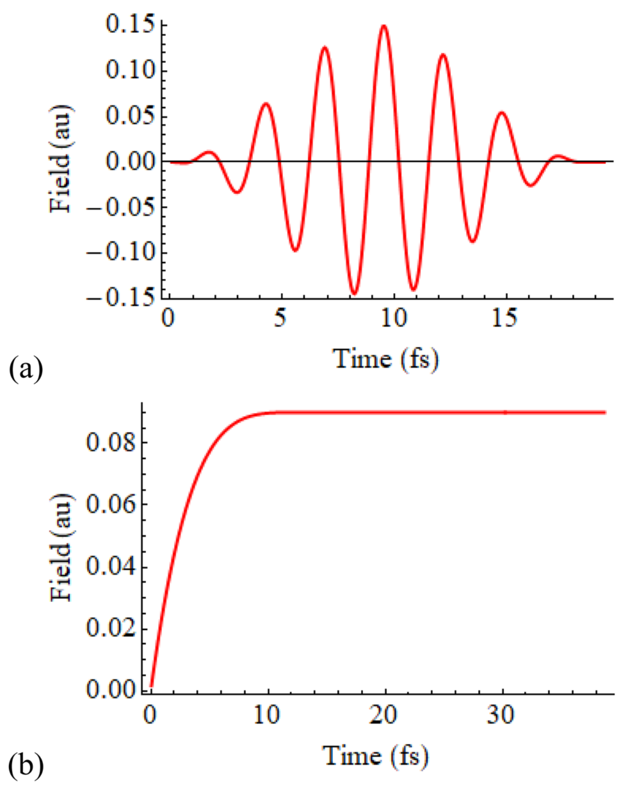

FIG. 1. (a) Seven cycle linearly polarized 800 nm pulse with a $\sin^2$ envelope [Eq. (14)]; (b) "static" pulse with electric field rising to a constant value [Eq. (16)].

for a linearly polarized pulse involves two full matrix-vector multiplies ($\mathbf{U}$ and $\mathbf{U}^T$) and three diagonal matrix-vector multiplies [$\exp(-i\,\mathbf{H}_{el}\Delta t/2)$ and $\exp(i\,E(t+\Delta t/2)\,\mathbf{d}\,\Delta t)$]. Because the propagation uses the exponential of the Hamiltonian, a fairly large time step of $\Delta t = 0.05$ a.u. (1.2 as) can be used. In similar simulations,[27] reducing the time step by a factor of 2 changed the ionization yield by less than 0.01%.

The corresponding Trotter factorization for a circularly polarized pulse involves two oscillating fields,

$$\begin{aligned}\mathbf{C}(t+\Delta t) = {} & \exp(-i\,\mathbf{H}_{el}\Delta t/2)\exp(-\mathbf{V}^{absorb}\Delta t/2)\\ & \times \mathbf{W}_2^T\exp(i\,E_2(t+\Delta t/2)\,\mathbf{d}_2\,\Delta t/2)\,\mathbf{W}_2\\ & \times \mathbf{W}_1^T\exp(i\,E_1(t+\Delta t/2)\,\mathbf{d}_1\,\Delta t)\,\mathbf{W}_1\\ & \times \mathbf{W}_2^T\exp(i\,E_2(t+\Delta t/2)\,\mathbf{d}_2\,\Delta t/2)\,\mathbf{W}_2\\ & \times \exp(-\mathbf{V}^{absorb}\Delta t/2)\exp(-i\,\mathbf{H}_{el}\Delta t/2)\mathbf{C}(t),\end{aligned} \tag{18}$$

where $\mathbf{W}_1\mathbf{D}_1\mathbf{W}_1{}^T = \mathbf{d}_1$ and $\mathbf{W}_2\mathbf{D}_2\mathbf{W}_2{}^T = \mathbf{d}_2$ are the eigenvalues and eigenvectors of the transition dipole matrices $\mathbf{D}_1$ and $\mathbf{D}_2$ in the two orthogonal field directions. A propagation step for a circularly polarized pulse involves four full matrix-vector multiplies and five diagonal matrix-vector multiplies.

The results of the simulations can be analyzed by examining the one electron density and orbital populations of the propagated wavefunction, $\Psi(t)/|\Psi(t)|$, and the absorbed wavefunction, $\hat{\mathbf{V}}^{absorb}\Psi(t)\,/|\hat{\mathbf{V}}^{absorb}\Psi(t)|$. Additional details can be obtained by projecting the absorbed wavefunction onto the individual ionized states, $\langle\Psi^I|\hat{\mathbf{V}}^{absorb}|\Psi(t)\rangle/|\hat{\mathbf{V}}^{absorb}\Psi(t)|$. The ionized states, $\Psi^I = \sum_x c_x^I\Psi_x$ for CIS and $\Psi^I = \sum_{xy} c_{xy}^I\Psi_{xy}$ for CISD-IP, are calculated as eigenfunctions of the field-free Hamiltonian plus spin–orbit coupling, $\hat{\mathbf{H}}_{el} + \hat{\mathbf{V}}^{SOC}$, using the same molecular orbitals as the CIS and CISD-IP wavefunctions. In terms of the matrix elements of the absorbing potential, the projections of the CIS and CISD-IP wavefunctions can be written as

$$\langle\Psi^I|\hat{\mathbf{V}}^{absorb}|\Psi(t)\rangle = \sum_{xa,jb} c_x^{I^*} c_j^b(t)\langle\Psi_x^a|\hat{\mathbf{V}}^{absorb}|\Psi_j^b\rangle$$

and (19)

$$\langle\Psi^I|\hat{\mathbf{V}}^{absorb}|\Psi(t)\rangle = \sum_{xa,jb} c_{xy}^{I^*} c_{jy}^b(t)\langle\Psi_x^a|\hat{\mathbf{V}}^{absorb}|\Psi_{jy}^b\rangle.$$

TABLE I. Spin–orbit splitting (eV) calculated with CISD-IP.

	Calc.[a]	Calc.[b]	Calc.[c]	Expt.[d]	Opt. Z^{eff} [e]	Opt. Z^{eff} [f]
Ar^+ ($^2P_{1/2}$–$^2P_{3/2}$)	0.1637	0.1654	0.177	0.177	16.1283	16.8492
Kr^+ ($^2P_{1/2}$–$^2P_{3/2}$)	0.4408	0.6006	0.666	0.666	36.3112	36.2462
Xe^+ ($^2P_{1/2}$–$^2P_{3/2}$)	2.4972	1.8597	1.306	1.306	36.0657	36.0317
HCl^+ ($^2\Pi_{1/2}$–$^2\Pi_{3/2}$)	0.0749	0.0735	0.0804	0.0804	15.2877	15.2499
HBr^+ ($^2\Pi_{1/2}$–$^2\Pi_{3/2}$)	0.2291	0.2959	0.3289	0.3289	35.3165	35.2944
HI^+ ($^2\Pi_{1/2}$–$^2\Pi_{3/2}$)	1.0872	0.8195	0.6695	0.6695	37.7047	37.4885

[a]CISD-IP/aug-cc-pVTZ using Z^{eff} from Ref. 49.
[b]CISD-IP/aug-cc-pVTZ using Z^{eff} from Ref. 72.
[c]Present work with CISD-IP/aug-cc-pVTZ and CISD-IP/aug-cc-pVTZ + ABS using Z^{eff} optimized to reproduce the experimental values.
[d]Reference 79.
[e]Present work for CISD-IP/aug-cc-pVTZ.
[f]Present work for CISD-IP/aug-cc-pVTZ + ABS.

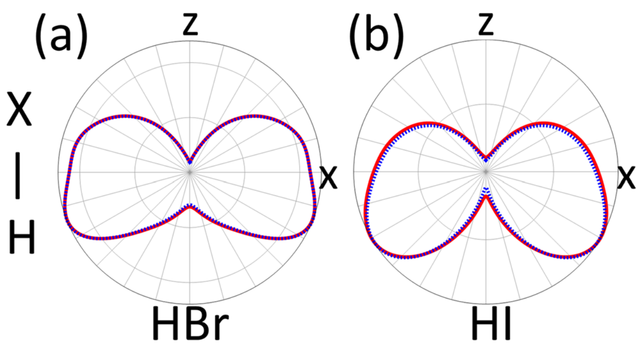

FIG. 2. Angular dependence of the ionization yield in the xz plane for (a) HBr and (b) HI with spin–orbit coupling (red solid line) and without spin–orbit coupling (blue dashed line) using a static pulse [Eq. (16)] with E_{max} = 0.05 a.u. for HBr and E_{max} = 0.04 a.u. for HI. The relative ionization yield is plotted radially, and the angle corresponds to minus the direction of the field (i.e., the direction the electron is ejected); the orientation of HX is shown on the left (aligned with the z axis, halogen in the +z direction).

A locally modified version of the Gaussian software package[73] was used to calculate the integrals needed for the TDCI simulation. Bond lengths for HCl, HBr, and HI were 1.3147 Å, 1.4484 Å, and 1.6200 Å. The aug-cc-pVTZ basis set[74–76] was used for H, Cl, Br, Ar, and Kr. Calculations for I and Xe used the all electron aug-cc-pVTZ-DK3 basis set[77] and the aug-cc-pVTZ-PP basis set with a pseudopotential to account for relativistic effects in the core.[78] Koseki, Gordon, and co-workers[49] obtained 1.00, 14.24, 14.9, 24.5, 24.12, 65.72, and 66.96 for Z^{eff} of H, Cl, Ar, Br, Kr, I, and Xe, respectively. Chiodo and Russo[72] obtained 13.9757, 15.0570, 31.7240, 32.7708, 49.5391, and 50.5656 for Cl, Ar, Br, Kr, I, and Xe, respectively. In each case, the four highest occupied orbitals (ns, np_x, np_y, np_z) were included in the spin–orbit coupling and TDCI calculations. For the simulations of strong field ionization, these basis sets were augmented with an additional absorbing basis set (designated ABS) consisting of diffuse functions placed on each atom (four s functions with exponents of 0.0256, 0.0128, 0.0064, and 0.0032; four p functions with exponents of 0.0256, 0.0128, 0.0064, and 0.0032; five d functions with exponents of 0.0512, 0.0256, 0.0128, 0.0064, and 0.0032; and two f functions with exponents of 0.0256 and 0.0128)[14,27] for adequate interaction

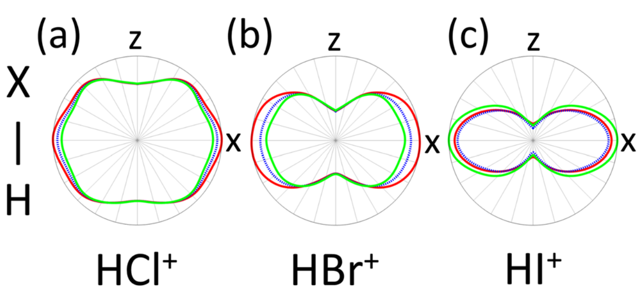

FIG. 3. Angular dependence of the ionization yield in the xz plane for (a) HCl^+, (b) HBr^+, and (c) HI^+ with spin–orbit coupling (red solid line for the $^2\Pi_{3/2}$ state, green solid line for the $^2\Pi_{1/2}$ state) and without spin–orbit coupling (blue dashed line for the $^2\Pi$ state) using a seven cycle linearly polarized 800 nm $\sin^2$ pulse [Eq. (14)] with E_{max} = 0.150 a.u. for HCl^+, E_{max} = 0.135 a.u. for HBr^+, and E_{max} = 0.090 a.u. for HI^+. The relative ionization yield is plotted radially, and the angle corresponds to minus the direction of the field (i.e., the direction the electron is ejected); the orientation of HX is shown on the left (aligned with the z axis, halogen in the +z direction).

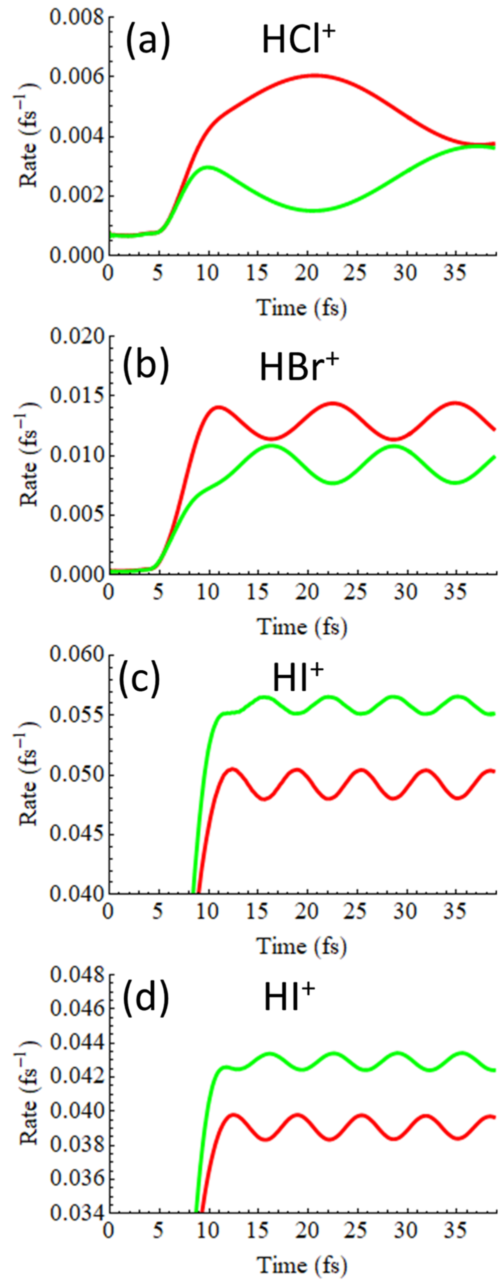

FIG. 4. Instantaneous ionization rates for strong field ionization starting from the $^2\Pi_{3/2}$ state (red) and starting from the $^2\Pi_{1/2}$ state (green) as a function of time for (a) HCl^+, (b) HBr^+, and (c) HI^+ using a static pulse [Eq. (16)] polarized perpendicular to the molecular axis and (d) HI^+ using a static pulse averaged over all orientations (E_{max} = 0.10 a.u. for HCl^+, E_{max} = 0.09 a.u. for HBr^+, and E_{max} = 0.08 a.u. for HI^+).

with the CAP. The time-dependent wavefunctions included all excitations from the two highest σ orbitals and two highest π orbitals to all virtual orbitals with orbital energies less than 3 hartree, for a total of 7960, 8408, and 8408 configurations for HCl^+, HBr^+, and HI^+, respectively. The TDCI simulations were carried out with an external Fortran 95 code.

III. RESULTS AND DISCUSSION

The calculated and experimental spin–orbit splittings for noble gas cations and hydrogen halide cations are summarized in Table I. The spin–orbit splittings are calculated with the CISD-IP/aug-cc-pVTZ level of theory using the approximated one electron spin–orbit coupling operator that depends on effective nuclear charges, Z^{eff}. Koseki, Gordon, and co-workers[49] estimated Z^{eff} from the MCSCF with the 6-31G(d,p) basis for elements up to Ar and with the 3-21G(d,p) basis for heavier elements. Chiodo and Russo[72] used RHF and B3LYP calculations with the DZVP basis set to obtain Z^{eff} for second through fifth row elements. Both show the correct trend, but calculations using Z^{eff} from the study of Chiodo and Russo are in much better agreement with the experimental values. For the TDCI simulations, it is desirable to have values for Z^{eff} that reproduce the experimental spin–orbit splitting for the systems of interest. In the absence of experimental data, Z^{eff} could be optimized to reproduce the results of accurate four-component relativistic calculations. The optimized Z^{eff} for the all electron aug-cc-pVTZ basis sets are listed in the second last column of Table I. Adding the absorbing basis to the aug-cc-pVTZ basis sets changes the optimized Z^{eff} by only a small amount (last column of Table I). For the lighter elements, Z^{eff} is close to Z. The larger difference seen for Xe^+ and HI^+ is most likely because the Hartree–Fock reference determinant used for the CISD-IP calculations neglects the relativistic effects for the core orbitals. These effects can be taken into account with relativistic pseudopotentials. The corresponding values of Z^{eff} for Xe^+ and HI^+ are 2409 and 2398 with the aug-cc-pVTZ-PP basis sets that use pseudopotentials to account for relativistic effects in the core. When the aug-cc-pVTZ-PP basis set is augmented with the absorbing basis, the optimized Z^{eff} for Xe^+ and HI^+ are 2424 and 2416.

The effect of spin–orbit coupling on the angular dependence of the ionization yield has been examined using the hydrogen halides and their cations. The ground states of the neutral hydrogen halides are singlets and are not subject to spin–orbit splitting. However, the excitation energies and ionization energies are affected by spin–orbit splitting. As shown in Fig. 2 for HBr and HI, the angular dependence

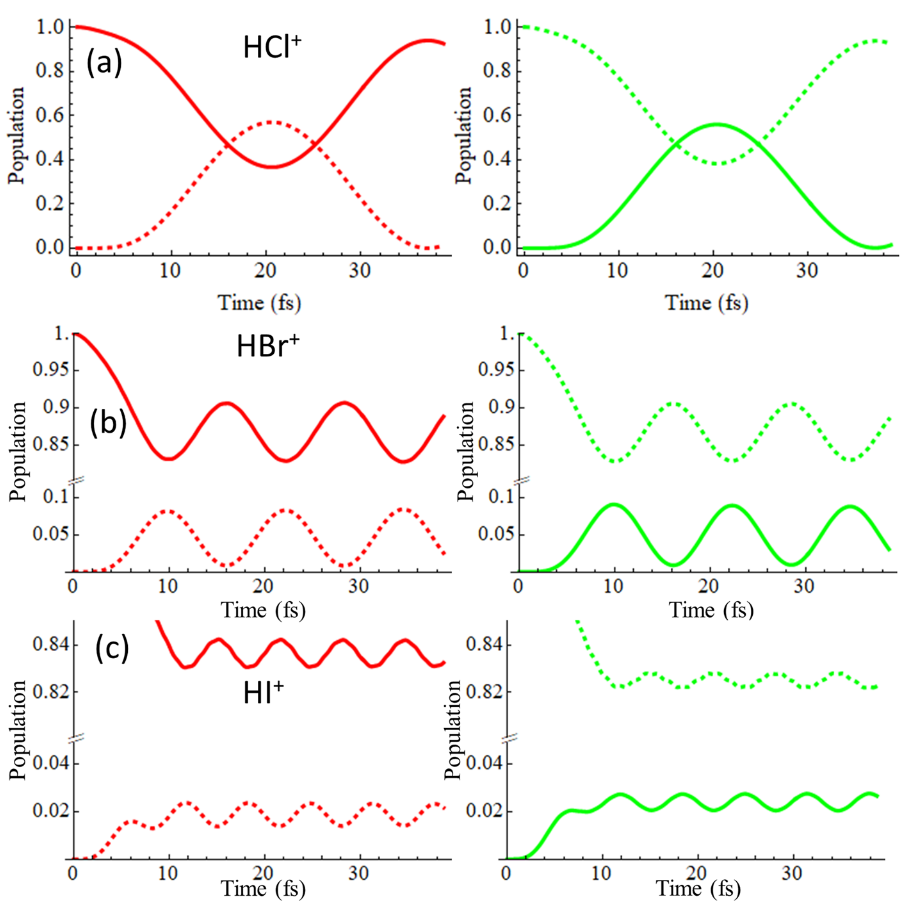

FIG. 5. Populations of the $^2\Pi_{3/2}$ field-free state (solid) and the $^2\Pi_{1/2}$ field-free state (dashed) as a function of time in the wavefunctions for strong field ionization starting from the $^2\Pi_{3/2}$ state (red) and starting from the $^2\Pi_{1/2}$ state (green) of (a) HCl^+, (b) HBr^+, and (c) HI^+ [using a static pulse, Eq. (14), polarized perpendicular to the molecular axis with E_{max} = 0.10 a.u. for HCl^+, E_{max} = 0.09 a.u. for HBr^+, and E_{max} = 0.08 a.u. for HI^+].

is nearly identical with and without spin–orbit coupling. The rotationally averaged ionization yield for HI is about 2.5% larger with spin–orbit coupling.

The hydrogen halide radical cations are better probes of the effect of spin–orbit coupling on strong field ionization. The s^2p^5 configuration of the valence shell is split into $^2\Pi_{3/2}$ and $^2\Pi_{1/2}$ states by spin–orbit coupling. Since HX^+ were used to obtain the optimized Z^{eff}, the calculated $^2\Pi_{3/2}$ and $^2\Pi_{1/2}$ energy differences match the experimental values in Table I. Figure 3 compares the ionization rate of the hydrogen halide cations with and without spin–orbit coupling. The simulation of strong field ionization was carried out using a seven cycle linearly polarized 800 nm pulse with a $\sin^2$ envelope. The rate was obtained by averaging the instantaneous rate over the central five cycles. As expected, population analysis of the absorbed wavefunction and projection onto the doubly ionized states confirm that ionization for polarizations perpendicular to the molecular axis is mainly from the π orbitals, while ionization for polarizations parallel to the molecular axis is dominated by removing an electron from the σ_p orbital. The largest effect of spin–orbit coupling is seen for polarizations perpendicular to the molecular axis. The difference between the ionization rates for the $^2\Pi_{3/2}$ and $^2\Pi_{1/2}$ states increases with the energy splitting between these states. When the field is parallel to the molecular axis, there is no difference in the ionization rates because the $^2\Pi_{3/2}$ and $^2\Pi_{1/2}$ states have a node along the axis. The rotationally averaged ionization yields for the $^2\Pi_{3/2}$ and $^2\Pi_{1/2}$ states of HI^+ are about 7% and 16% larger, respectively, than those without spin–orbit coupling.

More details of the effect of spin–orbit coupling on strong field ionization can be obtained by examining the rates and populations of the spin–orbit states as a function of time. A static field perpendicular to the molecular axis shows that the instantaneous rates oscillate as a function of time (Fig. 4). The oscillations are only slightly diminished by rotational averaging [Fig. 4(d) for HI^+]. The $^2\Pi_{3/2}$ and $^2\Pi_{1/2}$ states are eigenfunctions of the field-free Hamiltonian but are no longer eigenstates when the field is turned on. As the field is ramped up to its final constant value, the initial states evolve into a coherent superposition of the eigenstates in the field. Figure 5 shows the populations of the field-free $^2\Pi_{3/2}$ and $^2\Pi_{1/2}$ states when the initial $^2\Pi_{3/2}$ and $^2\Pi_{3/1}$ wavefunctions are propagated in a field ramped from zero to a constant value [Eq. (16)]. The frequency of oscillation is determined by the difference in the energy of the $^2\Pi_{3/2}$ and $^2\Pi_{1/2}$ states in the field. For HI^+ and HBr^+, the energy gap in the field (0.636 eV and 0.337 eV, respectively) is nearly the same as the gap in the absence of the field (0.6695 eV and 0.3289 eV, respectively). Because the energy difference for HCl^+ is small, the field strength affects the energy difference more significantly. Consequently, the oscillation frequency for HCl^+ has a greater dependence on the final field strength (0.112 eV for a field of 0.10 a.u. vs 0.0804 eV for free field). The energy difference between the $^2\Pi_{3/2}$ and $^2\Pi_{1/2}$ states also affects the magnitudes of the oscillations in the populations. The smaller energy difference in HCl^+ leads to greater mixing and larger amplitudes, whereas the larger energy difference in HI^+ leads to less mixing and smaller amplitudes. The oscillations in the populations of the $^2\Pi_{3/2}$ and $^2\Pi_{1/2}$ states shown in Fig. 5 correspond to a time-dependent coherent superposition of a hole in the p_+ and p_- orbitals. This is equivalent to a hole rotating in the xy plane, which results in an oscillation of the ionization rate in the x direction as seen in Fig. 4.

For very short circularly polarized pulses, the instantaneous ionization rate depends on the carrier envelope phase. Figure 6 shows the ionization rate as a function of time for a circularly polarized pulse in the xz plane when the maximum in the electric field is perpendicular to the molecular axis. Ionization occurs from the π orbitals near the peak in the electric field. The difference in the ionization rate for the $^2\Pi_{3/2}$ and $^2\Pi_{1/2}$ states is greatest at the peak and, as expected, is larger for HI^+ than for HBr^+. Figure 7 shows the ionization rate when the maximum in the field is aligned with the molecular axis. At the maximum, ionization is predominantly from the σ orbitals because the π orbitals have a node along the molecular axis. The rate of ionization for the σ orbitals is lower than that for the π orbitals. However, a quarter cycle before and after the maximum,

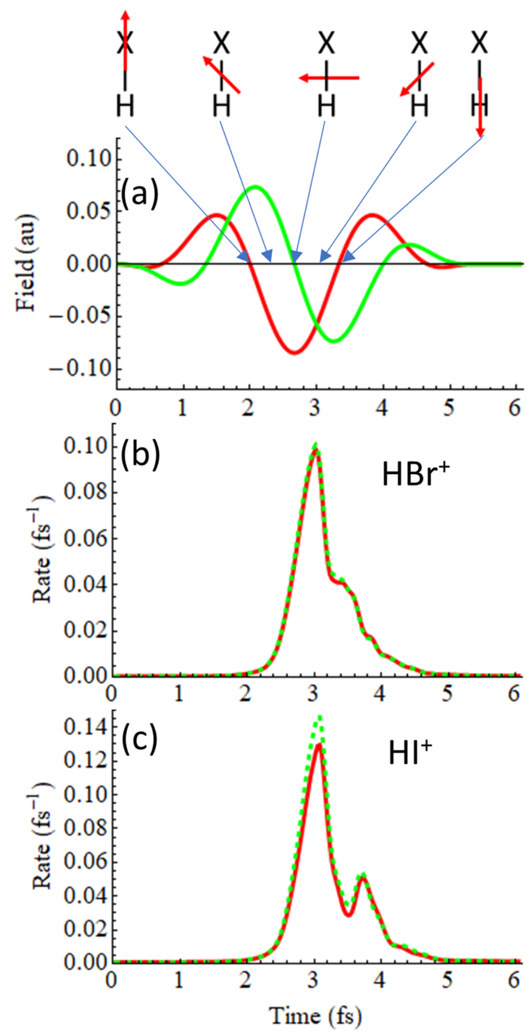

FIG. 6. Ionization rates for a two cycle circularly polarized pulse with a maximum along the −x axis [Eq. (15), γ = 0]: (a) x-component (red) and z-component (green), (b) ionization rate for the $^2\Pi_{3/2}$ state (red) and $^2\Pi_{1/2}$ state (green dashed) of HBr^+ as a function of time for E_{max} = 0.15 a.u., and (c) ionization rate for the $^2\Pi_{3/2}$ state (red) and $^2\Pi_{1/2}$ state (green dashed) of HI^+ as a function of time for E_{max} = 0.11 a.u.

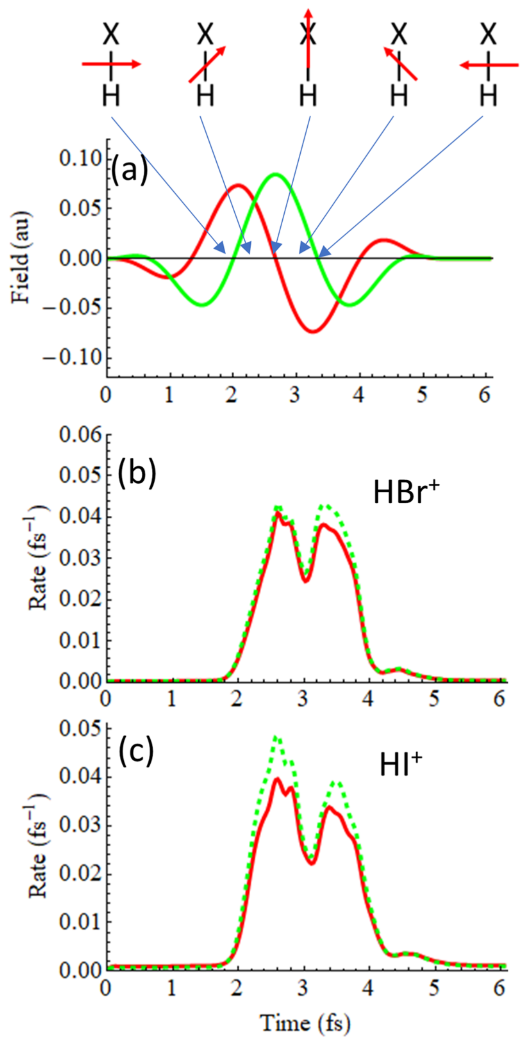

FIG. 7. Ionization rates for a two cycle circularly polarized pulse with a maximum along the +z axis [Eq. (15), $\gamma = \pi/2$]: (a) x-component (red) and z-component (green), (b) ionization rate for the $^2\Pi_{3/2}$ state (red) and $^2\Pi_{1/2}$ state (green dashed) of HBr^+ as a function of time for E_{max} = 0.15 a.u., and (c) ionization rate for the $^2\Pi_{3/2}$ state (red) and $^2\Pi_{1/2}$ state (green dashed) of HI^+ as a function of time for E_{max} = 0.11 a.u.

the field is aligned with the π orbital and the ionization rate increases even though the field is a little smaller than that at the maximum in the carrier envelope. As a result, the ionization rate as a function of time has a double peaked shape.

IV. SUMMARY

Strong field ionization by intense laser fields has been simulated with time-dependent configuration interaction with a complex absorbing potential. Spin–orbit coupling has been implemented in the TDCI Hamiltonian for CIS and CISD-IP wavefunctions using an effective one electron spin–orbit coupling operator. In the effective one electron spin–orbit coupling operator, Z^{eff} has been optimized for Ar^+, Kr^+, Xe^+, HX^+ (X = Cl, Br, and I). Spin–orbit effects on angular dependence of the strong field ionization have been studied for HX and HX^+ with a seven cycle linearly polarized pulse. The spin–orbit effects on ionization are small for HX since the ground states are closed shell. The effects are much larger for HX^+ because the spin–orbit coupling splits the ground states of HX^+ into $^2\Pi_{3/2}$ and $^2\Pi_{1/2}$ states. Consequently, the effects of spin–orbit coupling are largest for π orbitals in directions perpendicular to the molecular axis of HX^+. When a static field is applied by ramping it up from zero and holding it at a constant value, oscillations are seen between the $^2\Pi_{3/2}$ and $^2\Pi_{1/2}$ states of HX^+. For ionization of HX^+ by a two cycle circularly polarized pulse, a single peak is seen when the maximum in the carrier envelope is perpendicular to the molecular axis and two peaks are seen when it is parallel to the axis. This can be attributed to the greater ionization rate for the π orbitals than for the σ orbitals.

ACKNOWLEDGMENTS

The authors thank the Wayne State University computing grid for the computational time. This work was supported by a grant from the National Science Foundation (Grant No. CHE1856437).

The authors declare no competing financial interest.

DATA AVAILABILITY

The data that support the findings of this study are available from the corresponding author upon reasonable request.

REFERENCES

[1] M. Nisoli, P. Decleva, F. Calegari, A. Palacios, and F. Martín, "Attosecond electron dynamics in molecules," Chem. Rev. **117**, 10760 (2017).

[2] E. Goulielmakis *et al.*, "Real-time observation of valence electron motion," Nature **466**, 739 (2010).

[3] Y. Kobayashi, K. F. Chang, S. M. Poullain, V. Scutelnic, T. Zeng, D. M. Neumark, and S. R. Leone, "Coherent electronic-vibrational dynamics in deuterium bromide probed via attosecond transient-absorption spectroscopy," Phys. Rev. A **101**, 063414 (2020).

[4] K. L. Ishikawa and T. Sato, "A review on *ab initio* approaches for multielectron dynamics," IEEE J. Sel. Top. Quantum Electron. **21**, 8700916 (2015).

[5] J. J. Goings, P. J. Lestrange, and X. Li, "Real-time time-dependent electronic structure theory," Wiley Interdiscip. Rev.: Comput. Mol. Sci. **8**, e1341 (2018).

[6] A. Palacios and F. Martín, "The quantum chemistry of attosecond molecular science," Wiley Interdiscip. Rev.: Comput. Mol. Sci. **10**, e1430 (2020).

[7] P. Saalfrank, F. Bedurke, C. Heide, T. Klamroth, S. Klinkusch, P. Krause, M. Nest, and J. C. Tremblay, in *Advances in Quantum Chemistry*, edited by K. Ruud and E. J. Brändas (Academic Press, 2020), p. 15.

[8] S. Klinkusch, P. Saalfrank, and T. Klamroth, "Laser-induced electron dynamics including photoionization: A heuristic model within time-dependent configuration interaction theory," J. Chem. Phys. **131**, 114304 (2009).

[9] L. Greenman, P. J. Ho, S. Pabst, E. Kamarchik, D. A. Mazziotti, and R. Santra, "Implementation of the time-dependent configuration-interaction singles method for atomic strong-field processes," Phys. Rev. A **82**, 023406 (2010).

[10] M. Nest, T. Klamroth, and P. Saalfrank, "*Ab initio* electron dynamics with the multi-configuration time-dependent Hartree-Fock method," Z. Phys. Chem. **224**, 569 (2010).

[11] C. Huber and T. Klamroth, "Explicitly time-dependent coupled cluster singles doubles calculations of laser-driven many-electron dynamics," J. Chem. Phys. **134**, 054113 (2011).

[12]J. C. Tremblay, S. Klinkusch, T. Klamroth, and P. Saalfrank, "Dissipative many-electron dynamics of ionizing systems," J. Chem. Phys. **134**, 044311 (2011).
[13]T. Sato and K. L. Ishikawa, "Time-dependent complete-active-space self-consistent-field method for multielectron dynamics in intense laser fields," Phys. Rev. A **88**, 023402 (2013).
[14]P. Krause, J. A. Sonk, and H. B. Schlegel, "Strong field ionization rates simulated with time-dependent configuration interaction and an absorbing potential," J. Chem. Phys. **140**, 174113 (2014).
[15]S. Bauch, L. K. Sørensen, and L. B. Madsen, "Time-dependent generalized-active-space configuration-interaction approach to photoionization dynamics of atoms and molecules," Phys. Rev. A **90**, 062508 (2014).
[16]A. Karamatskou, S. Pabst, Y.-J. Chen, and R. Santra, "Calculation of photoelectron spectra within the time-dependent configuration-interaction singles scheme," Phys. Rev. A **89**, 033415 (2014).
[17]H. Miyagi and L. Bojer Madsen, "Time-dependent restricted-active-space self-consistent-field singles method for many-electron dynamics," J. Chem. Phys. **140**, 164309 (2014).
[18]S. Pabst and R. Santra, "Spin-orbit effects in atomic high-harmonic generation," J. Phys. B: At., Mol. Opt. Phys. **47**, 124026 (2014).
[19]S. Chattopadhyay, S. Bauch, and L. B. Madsen, "Electron-correlation effects in enhanced ionization of molecules: A time-dependent generalized-active-space configuration-interaction study," Phys. Rev. A **92**, 063423 (2015).
[20]P. Krause and H. B. Schlegel, "Angle-dependent ionization of small molecules by time-dependent configuration interaction and an absorbing potential," J. Phys. Chem. Lett. **6**, 2140 (2015).
[21]P. Krause and H. B. Schlegel, "Angle-dependent ionization of hydrides AH_n calculated by time-dependent configuration interaction with an absorbing potential," J. Phys. Chem. A **119**, 10212 (2015).
[22]R. Sawada, T. Sato, and K. L. Ishikawa, "Implementation of the multiconfiguration time-dependent Hatree-Fock method for general molecules on a multiresolution Cartesian grid," Phys. Rev. A **93**, 023434 (2016).
[23]D. Toffoli and P. Decleva, "A multichannel least-squares B-spline approach to molecular photoionization: Theory, implementation, and applications within the configuration-interaction singles approximation," J. Chem. Theory Comput. **12**, 4996 (2016).
[24]E. Lotstedt, T. Kato, and K. Yamanouchi, in *Progress in Ultrafast Intense Laser Science XIII*, edited by K. Yamanouchi, W. T. Hill, and G. G. Paulus (Springer, Cham, 2017), p. 15.
[25]V. P. Majety and A. Scrinzi, "Multielectron effects in strong-field ionization of CO_2: Impact on differential photoelectron spectra," Phys. Rev. A **96**, 053421 (2017).
[26]A. H. Winney, S. K. Lee, Y. F. Lin, Q. Liao, P. Adhikari, G. Basnayake, H. B. Schlegel, and W. Li, "Attosecond electron correlation dynamics in double ionization of benzene probed with two-electron angular streaking," Phys. Rev. Lett. **119**, 123201 (2017).
[27]P. Hoerner and H. B. Schlegel, "Angular dependence of strong field ionization of CH_3X (X = F, Cl, Br, or I) using time-dependent configuration interaction with an absorbing potential," J. Phys. Chem. A **121**, 5940 (2017).
[28]P. Hoerner and H. B. Schlegel, "Angular dependence of ionization by circularly polarized light calculated with time-dependent configuration interaction with an absorbing potential," J. Phys. Chem. A **121**, 1336 (2017).
[29]P. Hoerner and H. B. Schlegel, "Angular dependence of strong field ionization of haloacetylenes HCCX (X = F, Cl, Br, I), using time-dependent configuration interaction with an absorbing potential," J. Phys. Chem. C **122**, 13751 (2018).
[30]A. H. Winney, G. Basnayake, D. A. Debrah, Y. F. Lin, S. K. Lee, P. Hoerner, Q. Liao, H. B. Schlegel, and W. Li, "Disentangling strong-field multielectron dynamics with angular streaking," J. Phys. Chem. Lett. **9**, 2539 (2018).
[31]S. Chattopadhyay and L. B. Madsen, "Electron correlation effects in enhanced ionization of diatomic molecules in near-infrared fields," Phys. Rev. A **99**, 023424 (2019).
[32]P. Hoerner, M. K. Lee, and H. B. Schlegel, "Angular dependence of strong field ionization of N_2 by time-dependent configuration interaction using density functional theory and the Tamm-Dancoff approximation," J. Chem. Phys. **151**, 054102 (2019).
[33]P. Hoerner, W. Li, and H. B. Schlegel, "Angular dependence of strong field ionization of 2-phenylethyl-N,N-dimethylamine (PENNA) using time-dependent configuration interaction with an absorbing potential," J. Phys. Chem. A **124**, 4777 (2020).
[34]M. K. Lee, W. Li, and H. B. Schlegel, "Angular dependence of strong field sequential double ionization for neon and acetylene simulated with time-dependent configuration interaction using CIS and CISD-IP," J. Chem. Phys. **152**, 064106 (2020).
[35]X. Chu and S.-I. Chu, "Time-dependent density-functional theory for molecular processes in strong fields: Study of multiphoton processes and dynamical response of individual valence electrons of N_2 in intense laser fields," Phys. Rev. A **64**, 063404 (2001).
[36]X. Chu and S.-I. Chu, "Role of the electronic structure and multielectron responses in ionization mechanisms of diatomic molecules in intense short-pulse lasers: An all-electron *ab initio* study," Phys. Rev. A **70**, 061402 (2004).
[37]X. Chu and M. McIntyre, "Comparison of the strong-field ionization of N_2 and F_2: A time-dependent density-functional-theory study," Phys. Rev. A **83**, 013409 (2011).
[38]E. P. Fowe and A. D. Bandrauk, "Nonlinear time-dependent density functional theory studies of the ionization of CO_2 by ultrashort intense laser pulses(1)," Can. J. Chem. **87**, 1081 (2009).
[39]K. Lopata and N. Govind, "Modeling fast electron dynamics with real-time time-dependent density functional theory: Application to small molecules and chromophores," J. Chem. Theory Comput. **7**, 1344 (2011).
[40]A. Sissay, P. Abanador, F. Mauger, M. Gaarde, K. J. Schafer, and K. Lopata, "Angle-dependent strong-field molecular ionization rates with tuned range-separated time-dependent density functional theory," J. Chem. Phys. **145**, 094105 (2016).
[41]A. Bruner, S. Hernandez, F. Mauger, P. M. Abanador, D. J. LaMaster, M. B. Gaarde, K. J. Schafer, and K. Lopata, "Attosecond charge migration with TDDFT: Accurate dynamics from a well-defined initial state," J. Phys. Chem. Lett. **8**, 3991 (2017).
[42]P. Sandor *et al.*, "Angle dependence of strong-field single and double ionization of carbonyl sulfide," Phys. Rev. A **98**, 043425 (2018).
[43]P. Sandor *et al.*, "Angle-dependent strong-field ionization of halomethanes," J. Chem. Phys. **151**, 194308 (2019).
[44]K. G. Dyall and K. Fægri, *Introduction to Relativistic Quantum Chemistry* (Oxford University Press, New York, 2007).
[45]M. Reiher and A. Wolf, *Relativistic Quantum Chemistry: The Fundamental Theory of Molecular Science* (Wiley VCH, Weinheim, 2009).
[46]C. M. Marian, "Spin-orbit coupling and intersystem crossing in molecules," Wiley Interdiscip. Rev.: Comput. Mol. Sci. **2**, 187 (2012).
[47]C. M. Marian, in *Reviews in Computational Chemistry*, edited by K. B. Lipkowitz and D. B. Boyd (John Wiley & Sons, Inc., 2001), Vol. 17, p. 99.
[48]S. Koseki, M. W. Schmidt, and M. S. Gordon, "MCSCF/6-31G(D,P) calculations of one-electron spin-orbit-coupling constants in diatomic-molecules," J. Phys. Chem. **96**, 10768 (1992).
[49]S. Koseki, M. S. Gordon, M. W. Schmidt, and N. Matsunaga, "Main-group effective nuclear charges for spin-orbit calculations," J. Phys. Chem. **99**, 12764 (1995).
[50]S. Koseki, M. W. Schmidt, and M. S. Gordon, "Effective nuclear charges for the first- through third-row transition metal elements in spin-orbit calculations," J. Phys. Chem. A **102**, 10430 (1998).
[51]S. Koseki, D. G. Fedorov, M. W. Schmidt, and M. S. Gordon, "Spin-orbit splittings in the third-row transition elements: Comparison of effective nuclear charge and full Breit-Pauli calculations," J. Phys. Chem. A **105**, 8262 (2001).
[52]A. Berning, M. Schweizer, H.-J. Werner, P. J. Knowles, and P. Palmieri, "Spin-orbit matrix elements for internally contracted multireference configuration interaction wavefunctions," Mol. Phys. **98**, 1823 (2000).
[53]M. Kleinschmidt, J. Tatchen, and C. M. Marian, "SPOCK.CI: A multireference spin-orbit configuration interaction method for large molecules," J. Chem. Phys. **124**, 124101 (2006).
[54]D. Ganyushin and F. Neese, "A fully variational spin-orbit coupled complete active space self-consistent field approach: Application to electron paramagnetic resonance g-tensors," J. Chem. Phys. **138**, 104113 (2013).

[55] S. Mai, T. Müller, F. Plasser, P. Marquetand, H. Lischka, and L. González, "Perturbational treatment of spin-orbit coupling for generally applicable high-level multi-reference methods," J. Chem. Phys. **141**, 074105 (2014).
[56] O. Christiansen, J. Gauss, and B. Schimmelpfennig, "Spin-orbit coupling constants from coupled-cluster response theory," Phys. Chem. Chem. Phys. **2**, 965 (2000).
[57] K. Klein and J. Gauss, "Perturbative calculation of spin-orbit splittings using the equation-of-motion ionization-potential coupled-cluster ansatz," J. Chem. Phys. **129**, 194106 (2008).
[58] F. Wang and J. Gauss, "Analytic second derivatives in closed-shell coupled-cluster theory with spin-orbit coupling," J. Chem. Phys. **131**, 164113 (2009).
[59] E. Epifanovsky, K. Klein, S. Stopkowicz, J. Gauss, and A. I. Krylov, "Spin-orbit couplings within the equation-of-motion coupled-cluster framework: Theory, implementation, and benchmark calculations," J. Chem. Phys. **143**, 064102 (2015).
[60] D. Bokhan, A. Perera, D. N. Trubnikov, and R. J. Bartlett, "Excitation energies with spin-orbit couplings using equation-of-motion coupled-cluster singles and doubles eigenvectors," J. Chem. Phys. **147**, 164118 (2017).
[61] D. Bokhan, D. N. Trubnikov, A. Perera, and R. J. Bartlett, "Spin-orbit splitted excited states using explicitly-correlated equation-of-motion coupled-cluster singles and doubles eigenvectors," Chem. Phys. Lett. **698**, 171 (2018).
[62] D. Bokhan, D. N. Trubnikov, A. Perera, and R. J. Bartlett, "Spin-orbit split ionized and electron-attached states using explicitly-correlated equation-of-motion coupled-cluster singles and doubles eigenvectors," Chem. Phys. Lett. **730**, 372 (2019).
[63] L. Cheng and J. Gauss, "Perturbative treatment of spin-orbit coupling within spin-free exact two-component theory," J. Chem. Phys. **141**, 164107 (2014).
[64] L. Cheng, F. Wang, J. F. Stanton, and J. Gauss, "Perturbative treatment of spin-orbit-coupling within spin-free exact two-component theory using equation-of-motion coupled-cluster methods," J. Chem. Phys. **148**, 044108 (2018).
[65] Z. Cao, F. Wang, and M. Yang, "Spin-orbit coupling with approximate equation-of-motion coupled-cluster method for ionization potential and electron attachment," J. Chem. Phys. **145**, 154110 (2016).
[66] Z. Cao, F. Wang, and M. Yang, "Coupled-cluster method for open-shell heavy-element systems with spin-orbit coupling," J. Chem. Phys. **146**, 134108 (2017).
[67] Z. Wang, Z. Tu, and F. Wang, "Equation-of-motion coupled-cluster theory for excitation energies of closed-shell systems with spin-orbit coupling," J. Chem. Theory Comput. **10**, 5567 (2014).
[68] Z. Wang, S. Hu, F. Wang, and J. Guo, "Equation-of-motion coupled-cluster method for doubly ionized states with spin-orbit coupling," J. Chem. Phys. **142**, 144109 (2015).
[69] Z. Wang and F. Wang, "Equation-of-motion coupled-cluster method for ionised states with spin-orbit coupling using open-shell reference wavefunction," Mol. Phys. **116**, 935 (2018).
[70] N. Bellonzi, G. R. Medders, E. Epifanovsky, and J. E. Subotnik, "Configuration interaction singles with spin-orbit coupling: Constructing spin-adiabatic states and their analytical nuclear gradients," J. Chem. Phys. **150**, 014106 (2019).
[71] A. A. Golubeva, P. A. Pieniazek, and A. I. Krylov, "A new electronic structure method for doublet states: Configuration interaction in the space of ionized $1h$ and $2h1p$ determinants," J. Chem. Phys. **130**, 124113 (2009).
[72] S. G. Chiodo and N. Russo, "One-electron spin-orbit contribution by effective nuclear charges," J. Comput. Chem. **30**, 832 (2009).
[73] M. J. Frisch, G. W. Trucks, H. B. Schlegel, G. E. Scuseria *et al.*, Gaussian 10, Revision I.09, Gaussian, Inc., Wallingford, CT, 2010.
[74] T. H. Dunning, "Gaussian-basis sets for use in correlated molecular calculations. I. The atoms boron through neon and hydrogen," J. Chem. Phys. **90**, 1007 (1989).
[75] D. E. Woon and T. H. Dunning, Jr., "Gaussian basis sets for use in correlated molecular calculations. III. The atoms aluminum through argon," J. Chem. Phys. **98**, 1358 (1993).
[76] K. A. Peterson, B. C. Shepler, D. Figgen, and H. Stoll, "On the spectroscopic and thermochemical properties of ClO, BrO, IO, and their anions," J. Phys. Chem. A **110**, 13877 (2006).
[77] D. H. Bross and K. A. Peterson, "Correlation consistent, Douglas-Kroll-Hess relativistic basis sets for the 5p and 6p elements," Theor. Chem. Acc. **133**, 1434 (2013).
[78] K. A. Peterson, D. Figgen, E. Goll, H. Stoll, and M. Dolg, "Systematically convergent basis sets with relativistic pseudopotentials. II. Small-core pseudopotentials and correlation consistent basis sets for the post-d group 16–18 elements," J. Chem. Phys. **119**, 11113 (2003).
[79] K. P. Huber and G. Herzberg, *Molecular Spectra and Molecular Structure. IV. Constants of Diatomic Molecules* (Van Nostrand Reinhold Company, New York, 1979).